



CO₂ methanation catalyzed by oriented MoS₂ nanoplatelets supported on few layers graphene

Ana Primo^a, Jinbao He^a, Bogdan Jurca^b, Bogdan Cojocaru^b, Cristina Bucur^c,
Vasile I. Parvulescu^{b,*}, Hermenegildo Garcia^{b,*}

^a Instituto Universitario de Tecnología Química, Consejo Superior de Investigaciones Científicas-Universitat Politècnica de Valencia, Universitat Politècnica de Valencia, Av. De los Naranjos s/n, 46022 Valencia, Spain

^b Department of Organic Chemistry, Biochemistry and Catalysis, Faculty of Chemistry, University of Bucharest, Bdul Regina Elisabeta 4-12, Bucharest 030016, Romania

^c National Institute of Materials Physics, Str. Atomistilor 405A, P.O. Box MG7, 077125 Magurele, Romania

ARTICLE INFO

Keywords:

Heterogeneous catalysis

CO₂ methanation

Graphene as support

MoS₂ as hydrogenation catalyst

ABSTRACT

Powders of molybdenum disulfide platelets strongly grafted on graphene have been prepared by pyrolysis of ammonium alginate containing adsorbed various proportions of (NH₄)₂MoS₄. After pyrolysis, formation of MoS₂ supported on graphene was determined by XRD and electron microscopy and spectroscopic techniques. MoS₂/G exhibits catalytic activity for the methanation of CO₂, the performance being optimal at intermediate loadings. The catalytic activity of sharply contrasts with that of bulk MoS₂ that promotes the reverse water gas shift, affording CO as the main product. Characterization of the spent MoS₂/G catalyst shows the partial conversion of external MoS₂ into MoO₃. Comparison of the catalytic activity of MoS₂/G with that of MoO₃/G shows that the latter is less efficient, but more selective for CO₂ methanation.

1. Introduction

In the context of diminishing atmospheric CO₂ emissions, one of the possibilities is utilization of CO₂ as feedstock for the production of fuels and other chemicals [1–4]. Hydrogenation is among the few CO₂ transformations that are thermodynamically downhill and this reaction renders products that can be used as fuels or bulk chemicals [5,6]. The hydrogen required in this process is expected to be available in large amounts from water electrolysis using renewable electricity [7–9]. In view of this future scenario, there is a large incentive in developing non-noble metal catalysts to perform CO₂ hydrogenation forming products with high selectivity and efficiency at adequate rates under suitable conditions [10,11].

Molybdenum oxides and chalcogenides have been proposed as alternative catalysts to platinum for a series of reactions, including hydrogen evolution in electrolysis, hydrodesulfuration and synthesis gas conversions [12–16]. All these reactions have in common hydrogen as the reaction product or reagent. The use of molybdenum disulfide supported on graphene for electrocatalytic hydrogen evolution has been considered a breakthrough in this area, since this composite material can exhibit catalytic performance close to that of Pt nanoparticles due to the combination of the electrical conductivity of graphenes and the catalytic activity of MoS₂ [17,18].

Molybdenum has also been investigated for the valorization of CO₂. Early in 1981, Saito and Anderson [19] studied the activity of a series of molybdenum compounds for the methanation of CO₂ including oxides, sulfide, metal, carbide, and nitride, showing much higher reaction rates for MoO₃ than for Mo sulphides. While iron deactivated rapidly, molybdenum produced hydrocarbons in a certain extent and catalyzed the water gas-shift reaction. It was also demonstrated that in the presence of molybdenum, coke is not formed due to the efficient hydrogenation of the carbonaceous deposits [20]. On the other hand, MoS₂ has been used as support of Pt nanoparticles in the hydrogenation of CO₂, mainly to methanol [21].

Density functional theory (DFT) employed to investigate the methanol synthesis from CO₂ and H₂ on a Mo₆S₈ cluster (the structural building block of the Chevrel phase of molybdenum sulfide) indicated that MoS₂ can promote the C–O scission of H_xCO intermediates, thus explaining the high selectivity of molybdenum sulfides for the production of hydrocarbons. In contrast, the Mo₆S₈ cluster is predicted to have moderate activity for converting CO₂ and H₂ to methanol. Both the Mo and S sites participate in the reaction with CO₂, CO, and CH_xO, being Mo preferentially the binding sites, whereas S atoms facilitate H–H bond cleavage by forming relatively strong S–H bonds. The unexpected activity of the Mo₆S₈ cluster was considered to be the result of the interplay between shifts in the Mo d-band and S p-band in a unique

* Corresponding authors.

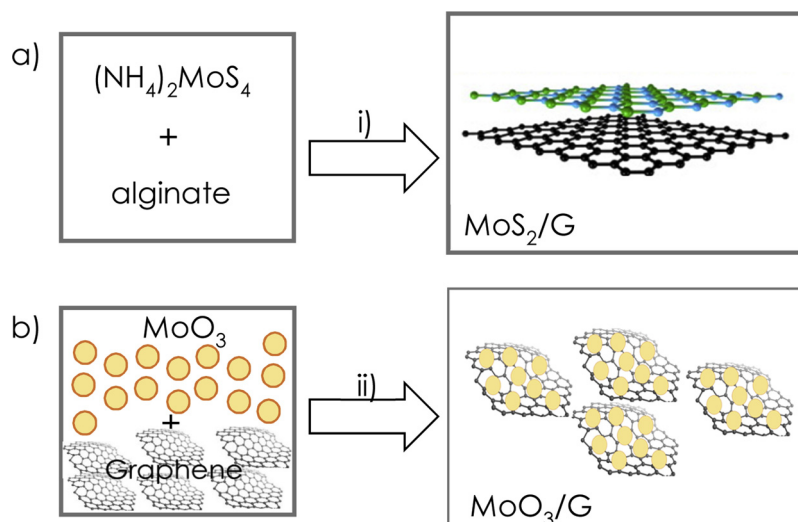
E-mail addresses: vasile.parvulescu@chimie.unibuc.ro (V.I. Parvulescu), hgarcia@qim.upv.es (H. Garcia).

<https://doi.org/10.1016/j.apcatb.2018.12.034>

Received 7 July 2018; Received in revised form 4 December 2018; Accepted 14 December 2018

Available online 15 December 2018

0926-3373/© 2018 Elsevier B.V. All rights reserved.



Scheme 1. Pictorial illustration for the preparation of a) MoS_2/G and b) MoO_3/G .

Table 1

List of samples prepared in the present study, relevant composition data and average particle.

Sample	MoS_2 or MoO_3 (wt%)	Particle size (nm)
G	–	–
MoS_2 -1/G	0.9	200–350
MoS_2 -2/G	2.4	200–350
MoS_2 -3/G	4.2	200–400
MoS_2 -4/G	12.7	250–400
MoO_3 -1/G	0.54	14.96
MoO_3 -2/G	6.24	22.86
MoO_3 -3/G	11.23	40.69

cage-like geometry [22]. The catalytic activity of MoS_2 surface for CO hydrogenation has also been studied by DFT and calculations suggest that the active sites correspond to edge Mo atoms adsorbing CO [23].

The association of molybdenum with carbon has also been indicated as beneficial by both experimental results and theoretical calculations. Thus, Cu- $\text{Mo}_2\text{C}/\text{MCM-41}$ was tested for CO_2 hydrogenation to form methanol. The activity of this catalyst was associated to a strong synergistic effect between Cu and Mo_2C , which also resulted in a higher selectivity for methanol [24]. Au and Cu, were also associated to molybdenum carbide ($\text{Au}/\delta\text{-MoC}$ and $\text{Cu}/\delta\text{-MoC}$) catalysts affording high activity, selectivity, and stability for the reduction of CO_2 to CO with some subsequent selective hydrogenation toward methanol. A detailed comparison of the behavior of $\text{Au}/\beta\text{-Mo}_2\text{C}$ and $\text{Au}/\delta\text{-MoC}$ catalysts also based on sophisticated experiments under controlled conditions and DFT calculations provided evidence of the impact of the metal/carbon ratio in the carbide on the performance of the catalysts [25]. DFT calculations also differentiate between the $\text{Mo}_2\text{C}(001)$ and $\text{Mo}_2\text{C}(101)$ surfaces, the latter affording an effective barrier allowing the surface C hydrogenation on the $\text{Mo}_2\text{C}(101)$ surface activated by the presence of 2O and 2OH pre-covered surfaces [26]. The reverse water–gas shift reaction is also catalyzed by potassium-promoted molybdenum carbide supported on $\gamma\text{-Al}_2\text{O}_3$ ($\text{K-Mo}_2\text{C}/\gamma\text{-Al}_2\text{O}_3$) [27]. DFT calculations have also been carried out for two-dimensional transition-metal carbides as CO_2 conversion catalysts. Among these Mo_3C_2 was found to exhibit a very promising CO_2 to CH_4 selective conversion capability. Calculations predicted the formation of OCHO^\cdot and HOCO^\cdot radical species in the early hydrogenation steps through spontaneous reactions [28].

Continuing with the use of molybdenum disulfide supported on graphene as catalyst, we have reported recently the preparation in one step of samples of few layers MoS_2 platelets supported on few-layers graphene (MoS_2/G) by pyrolysis at 900°C under inert atmosphere of

natural polysaccharides containing ammonium molybdotetrasulfide [29]. In this process a spontaneous segregation of graphene and MoS_2 takes places during the thermal restructuring of the polysaccharide forming graphene and carbochemical reduction of $(\text{NH}_4)_2\text{MoS}_4$ becoming precursor of MoS_2 . The resulting MoS_2/G is a photocatalyst for hydrogen generation from water in the presence of sacrificial electron donors and using Eosin Y as photosensitizer and also for the electrocatalytic H_2 evolution reaction [29]. Further characterization when the MoS_2/G heterojunction is prepared as film has revealed that the MoS_2 nanoplatelets with lateral dimensions between 15 and 105 nm and height between 5 and 15 nm, depending on MoS_2 loading, are preferentially oriented in the 0.02 crystallographic facet [30]. This preferential orientation is proposed to derive from the lattice matching of this MoS_2 crystallographic facet with the graphene hexagonal arrangement.

Aimed at expanding the scope of MoS_2/G as catalyst and considering the above-commented interest in CO_2 hydrogenation and reports on the molybdenum catalysts, the present manuscript reports the catalytic activity of MoS_2/G for CO_2 methanation, comparing the performance of MoS_2/G with that of analogous MoO_3/G samples, prepared by impregnation of preformed MoO_3 nanoparticles on G. It will be shown that MoS_2/G is efficient in promoting the selective CO_2 methanation, but it undergoes a gradual deactivation attributable to the conversion of MoS_2 to MoO_3 that, although still active, is less efficient than the fresh disulfide.

2. Experimental section

2.1. Synthesis of MoS_2/G samples

Different amounts of $(\text{NH}_4)_2\text{MoS}_4$ (560, 280, 140, and 70 mg for the samples MoS_2/G 2:1, 3:1, 4:1 and 5:1, respectively) were dissolved in 10 ml of water. Then, 1.00 g of alginate acid is dissolved in the same solution with 0.5 ml of NH_4OH . When the mixture is well dissolved, the water is evaporated under reduced pressure and the resulting solid is pyrolysed under argon flow at 250°C for 2 h and, then, at 900°C for 2 h (5°C min^{-1} heating rate). After pyrolysis, the powder is ground and exfoliated in water using a 750 W Sonics Vibracell high intensity ultrasonic liquid processor for 1.5 h.

2.2. Synthesis of MoO_3/G samples

Alginate acid is pyrolyzed under argon flow at 250°C for 2 h and, then, at 900°C for 2 h (5°C min^{-1} heating rate). 300 mg of the obtained

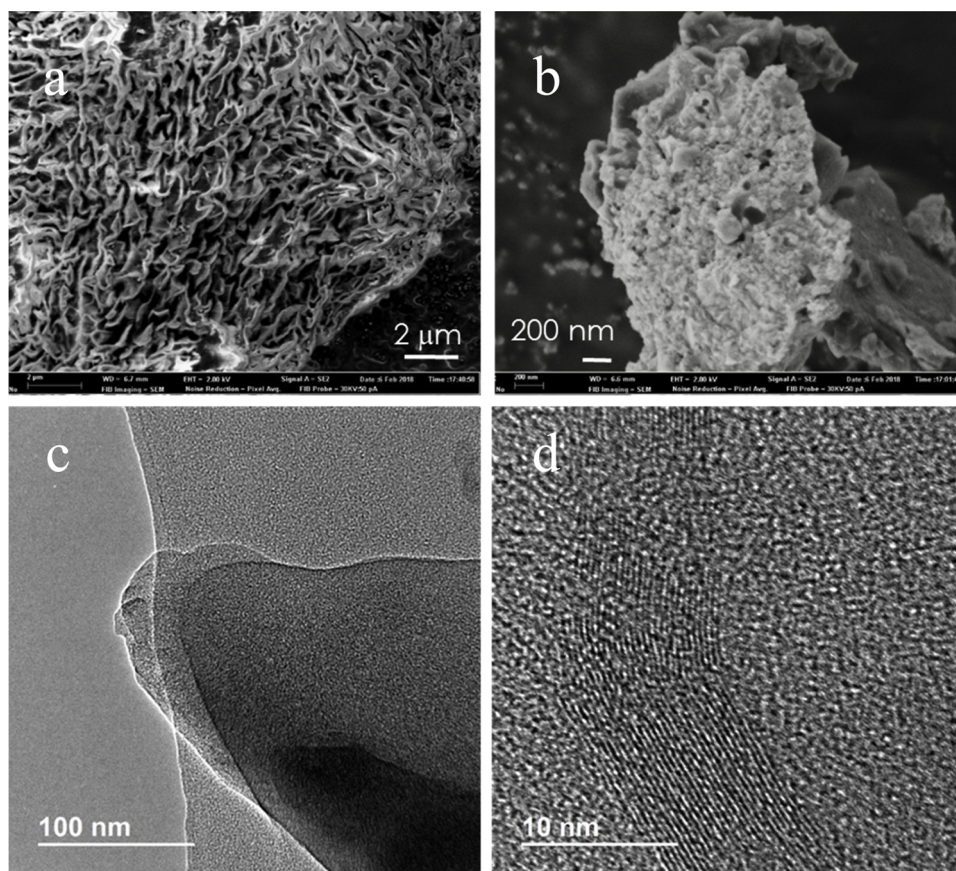


Fig. 1. Images of SEM (a and b) before sonication and TEM (c and d) after sonication corresponding to the MoS₂/G catalyst with the lowest MoS₂ loading.

carbonaceous residue is exfoliated in 300 mL of water using a 750 W Sonics Vibracell high intensity ultrasonic liquid processor for 1.5 h. Also, different amounts of commercial MoO₃ (15, 90 and 180 mg for the samples MoO₃-1/G, MoO₃-2/G and MoO₃-3/G, respectively) were sonicated in the same manner. Afterwards, the two suspensions were mixed and submitted to further sonication for 1.5 h. Then, the solid is filtered and washed with 1 L of deionized water and, finally, dried under vacuum overnight.

2.3. Catalytic tests and kinetics

Catalytic tests were performed in a setup (Microactivity tester, PID Eng&Tech) equipped with a stainless steel (316 SS) fixed bed tube reactor (Autoclave Engineers) featured with an inner K-type thermocouple. Two mass flow controllers (EL-FLOW Select, Bronkhorst) were used to feed the mixture of the inlet gases: hydrogen (5.0, Linde) and carbon dioxide (4.5, Linde). The total gas flow rate was checked before each experiment by help of a gas burette connected to the outlet of the reactor setup. An amount of 20 mg catalyst powder was introduced in the reactor; air was removed by flushing the system at room temperature for 15 min with 30 mL/min H₂ and 10 mL/min CO₂, followed by 30 min catalytic reaction at the flow rates of 3 mL/min H₂ and 1 mL/min CO₂. Afterwards, the reactor was pressurized at 10 bar. Five reaction temperatures between 300 and 500 °C were investigated. For each temperature, a set of three successive GC analyses were performed (at 5, 25 and 45 min after the stabilization of the temperature). The values of the CO₂ conversion obtained from the last two GC measurements coincided very well in all the experiments, indicating that the reactor setup reached the steady state operation conditions.

GC analyses were performed using H₂ as carrier gas on an Agilent 7890A chromatograph equipped with a capillary PLOT column (RT-Msieve 5A, Restek) and a TCD detector. Temperature program

considered a 5 min dwell at 50 °C, a ramp with 25°/min to 250 °C followed by a final dwell of 5 min, allowing thus a very good separation between CH₄, CO and CO₂. The gas samples were injected through a remotely controlled 6-way valve (A4C6WE, Vici) kept at ambient temperature. The reproducibility of the analysis system was checked prior to each experiment by injecting a series of three successive samples of gas mixture passed through the reactor at room temperature.

2.3.1. Estimation of the diffusion coefficients

The reaction mixture has been treated as a pentacomponent (CO₂, H₂, CH₄, CO, H₂O) real gas. The diffusion coefficient D_{im} of each component i in the gas mixture was estimated from the binary diffusion coefficients using Blanc's law (1):

$$D_{im} = \left(\sum_{i=1, j \neq i}^n \frac{x_j}{D_{ij}} \right)^{-1} \quad (1)$$

where:

D_{im} = diffusion coefficient of the component (i) in the gas mixture (m)

x_j = mole fraction of the component j

D_{ij} = binary diffusion coefficients for each ij components pair

Each D_{ij} coefficient was further estimated from Chapman-Enskog formula (2) or its Wilke-Lee modification (3):

$$D_{12} = \frac{0.00266 T^{3/2}}{P M_{12}^{1/2} \sigma_{12}^2 \Omega_D} \quad (2)$$

$$D_{12} = \frac{[3.03 - (0.98/M_{12}^{1/2})](10^{-3}) T^{3/2}}{P M_{12}^{1/2} \sigma_{12}^2 \Omega_D} \quad (3)$$

where:

D_{12} - binary diffusion coefficient, cm²/s

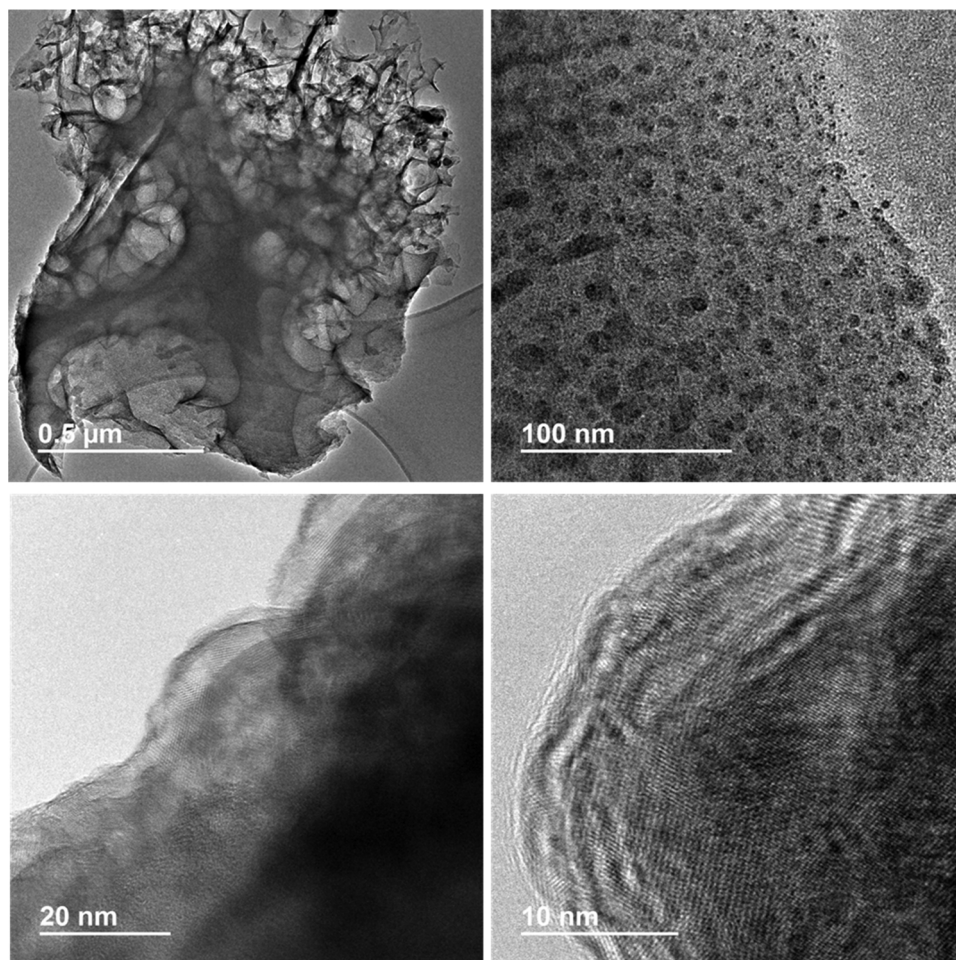


Fig. 2. Top: TEM images of MoO₃-2/G at different magnifications. Bottom: TEM images of G used to adsorb MoO₃ NPs.

T - absolute temperature, K

$M_{12} = 2\left(\frac{1}{M_1} + \frac{1}{M_2}\right)^{-1}$; M_1 , M_2 - molecular weights of components 1 and 2, g/mol

P - pressure, bar

$\sigma_{12} = (\sigma_1 + \sigma_2)/2$ - characteristic length (*i.e.* kinetic diameter) for binary collision between molecules of the components 1 and 2, Å

Ω_D - diffusion collision integral, dimensionless

The value of the collision integral Ω_D depends on the energy of intermolecular interactions which is commonly described by a 6–12 Lennard-Jones potential that depends on the characteristic length σ_{12} and the depth of the energy well ϵ . Tabulated data of σ_i (Å) and $\epsilon_i/k_{\text{Boltzmann}}$ (K) [31] for pure components were used to calculate σ_{ij} , $i \neq j$ (as arithmetic mean between σ_i and σ_j) and ϵ_{ij} , $i \neq j/k_B$ (as geometric mean between ϵ_i/k_B and ϵ_j/k_B); the last allows the calculation of the corresponding Ω_D integral using Neufeld parametrization [31]:

$$\Omega_D = \frac{A}{(T^*)^B} + \frac{C}{e^{DT^*}} + \frac{E}{e^{FT^*}} + \frac{G}{e^{HT^*}} \quad (4)$$

where: $T^* = k_B T / \epsilon_{ij}$; $A = 1.06036$; $B = 0.1561$; $C = 0.193$; $D = 0.47635$; $E = 1.03587$; $F = 1.52996$; $G = 1.76474$; $H = 3.89411$

The consistency of the parameterizations used in Chapman-Enskog and Wilke-Lee estimation methods was checked by calculating values of binary D_{12} coefficients (0 °C, 1 atm) and comparing the obtained values with experimental results [32]:

2.3.2. Calculation of the Weisz-Prater number

The adimensional Weisz-Prater criterion [33,34] is given by:

$$N_{W-P} = \frac{r_{\text{cat}} R_p^2}{C_s D_{\text{eff}}} \leq 0.3 \quad (5)$$

where:

r - reaction rate expressed per unit mass of catalyst, $\text{mol s}^{-1} (\text{g}^{-1})_{\text{cat}}$

ρ_{cat} - packed catalyst density, g cm^{-3}

R_p - catalyst particle radius, cm

C_s - concentration of the reactant at the surface of the catalyst particles, mol cm^{-3}

D_{eff} - effective diffusion coefficient, $\text{cm}^2 \text{s}^{-1}$

2.4. Characterization techniques

The Raman measurements (Horiba JobinYvon – Labram HR UV-vis-NIR 200–1600 nm Raman Microscope Spectrometer) were carried out at room temperature with the 633 nm line of a He-Ne ion laser as excitation source. XRD patterns were obtained in a Philips XPert diffractometer (40 kV and 45 mA) equipped with a graphite monochromator employing Ni-filtered Cu K α radiation (1.541178 Å). AFM images were made with a Multimode Nanoscope 3A equipment working in tapping mode, using mica as substrate. FESEM images were taken with an ULTRA 55 ZEISS Oxford instrument and HRTEM images with a JEM 2100F JEOL 200 kV electronic microscope.

3. Results and discussion

3.1. Sample preparation and characterization

Two types of materials, either MoS₂/G or MoO₃/G were prepared in

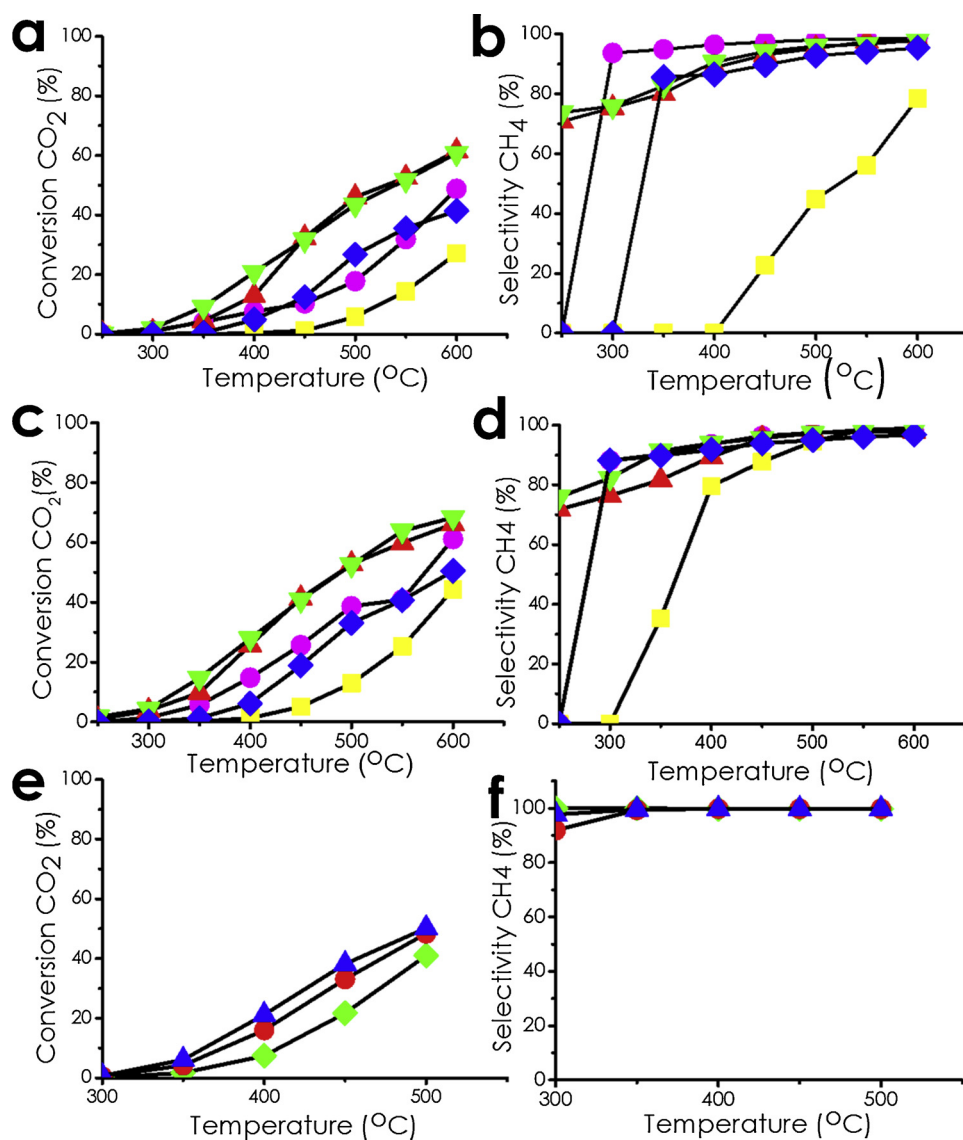


Fig. 3. Conversion (a, c and e) and methane selectivity (b, d and f) plots for CO₂ hydrogenation as a function of the temperature promoted by MoS₂/G or MoO₃/G catalysts as a function of loading. Legends: ■ G; ● MoS₂-1/G; ▲ MoS₂-2/G ▼ MoS₂-3/G ◇ MoS₂-4/G. Reaction conditions for a and b: P = 10 bar, Flow rates: H₂: 15 mL/min and CO₂: 5 mL/min, catalyst amount: 20 mg; Reaction conditions for c and d: Flow rates: H₂: 3 mL/min; CO₂: 1 mL/min Catalyst amount: 20 mg. Legends for plots e and f) ◆ MoO₃-1/G; ● MoO₃-2/G; ▲ MoO₃-3/G. Reaction conditions: P = 10 bar Flow rates: H₂: 3 mL/min; CO₂: 1 mL/min Catalyst amount: 20 mg.

Table 2

Values of the Weisz-Prater criterion for differential reaction conditions (CO₂ conversion < 5%), P = 10 bar, CO₂:H₂ (vol) = 1:3.

Catalyst	T (°C)	Total flow (mL/min)	C _{CO2} (mol/cm ³)	C _{H2} (mol/cm ³)	D _{CO2,m} (cm ² /s)	D _{H2,m} (cm ² /s)	$-r_{CO_2}$ mol/(s g _{cat})	N _{W-P} CO ₂	N _{W-P} H ₂
MoS ₂ -1/G	300	4	5.24·10 ⁻⁵	1.57·10 ⁻⁴	0.253	0.759	1.12·10 ⁻⁷	4.61·10 ⁻¹³	2.05·10 ⁻¹³
	300	20	5.18·10 ⁻⁵	1.55·10 ⁻⁴	0.241	0.734	4.09·10 ⁻⁶	1.79·10 ⁻¹¹	7.88·10 ⁻¹²
	350	4	4.70·10 ⁻⁵	1.39·10 ⁻⁴	0.260	0.802	1.86·10 ⁻⁶	8.30·10 ⁻¹²	3.65·10 ⁻¹²
	350	20	4.76·10 ⁻⁵	1.42·10 ⁻⁴	0.277	0.844	4.28·10 ⁻⁶	1.76·10 ⁻¹¹	7.78·10 ⁻¹²
MoS ₂ -2/G	300	4	5.12·10 ⁻⁵	1.53·10 ⁻⁴	0.233	0.718	1.41·10 ⁻⁶	6.59·10 ⁻¹²	2.86·10 ⁻¹²
	300	20	5.22·10 ⁻⁵	1.56·10 ⁻⁴	0.249	0.753	1.54·10 ⁻⁶	6.59·10 ⁻¹²	2.91·10 ⁻¹²
	350	20	4.70·10 ⁻⁵	1.40·10 ⁻⁴	0.265	0.817	8.13·10 ⁻⁶	3.63·10 ⁻¹¹	1.58·10 ⁻¹¹
MoS ₂ -3/G	300	4	5.14·10 ⁻⁵	1.53·10 ⁻⁴	0.235	0.722	1.23·10 ⁻⁶	6.31·10 ⁻¹²	2.75·10 ⁻¹²
	300	20	5.17·10 ⁻⁵	1.54·10 ⁻⁴	0.240	0.733	4.65·10 ⁻⁶	2.33·10 ⁻¹¹	1.02·10 ⁻¹¹
	350	20	4.79·10 ⁻⁵	1.43·10 ⁻⁴	0.283	0.856	2.79·10 ⁻⁶	2.13·10 ⁻¹¹	9.42·10 ⁻¹²
MoS ₂ -4/G	400	20	4.35·10 ⁻⁵	1.29·10 ⁻⁴	0.298	0.919	9.11·10 ⁻⁶	7.26·10 ⁻¹¹	3.19·10 ⁻¹¹
MoO ₃ -1/G	300	4	5.24·10 ⁻⁵	1.57·10 ⁻⁴	0.254	0.762	2.60·10 ⁻⁸	2.57·10 ⁻¹⁶	1.14·10 ⁻¹⁶
	350	4	4.78·10 ⁻⁵	1.43·10 ⁻⁴	0.281	0.852	6.32·10 ⁻⁷	6.18·10 ⁻¹⁵	2.73·10 ⁻¹⁵
MoO ₃ -2/G	300	4	5.23·10 ⁻⁵	1.57·10 ⁻⁴	0.252	0.758	1.48·10 ⁻⁷	3.83·10 ⁻¹⁵	1.70·10 ⁻¹⁵
	350	4	4.72·10 ⁻⁵	1.40·10 ⁻⁴	0.265	0.814	1.56·10 ⁻⁶	4.24·10 ⁻¹⁴	1.87·10 ⁻¹⁴
MoO ₃ -3/G	300	4	5.23·10 ⁻⁵	1.56·10 ⁻⁴	0.250	0.753	2.60·10 ⁻⁷	2.59·10 ⁻¹⁴	1.49·10 ⁻¹⁴
	350	4	4.67·10 ⁻⁵	1.37·10 ⁻⁴	0.254	0.787	2.27·10 ⁻⁶	2.49·10 ⁻¹³	1.09·10 ⁻¹³

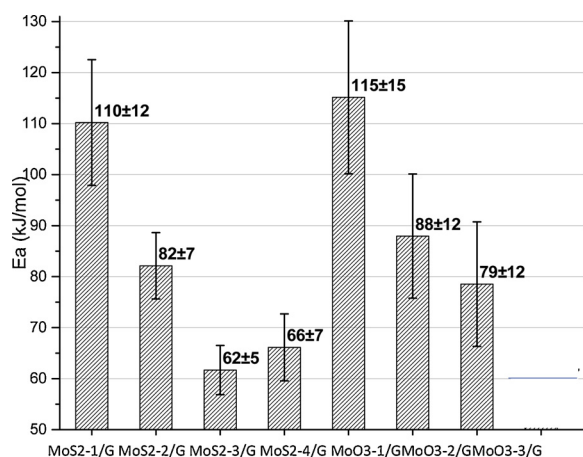


Fig. 4. Comparison between the activation energy values for the methanation process in presence of the investigated graphene-based catalysts. The error bars are calculated from the standard deviation of the slope for each $\ln(\text{CO}_2 \text{ conversion})$ vs. T^{-1} Arrhenius plot.

the present study to be tested as CO_2 hydrogenation catalysts. Scheme 1 illustrates the preparation procedure followed for each type of sample under study, while Table 1 summarizes relevant composition data and average particle size. As it can be seen there, the MoS_2/G samples were prepared by pyrolysis at 900°C of alginate containing different amounts of $(\text{NH}_4)_2\text{MoS}_4$ adsorbed on the fibrils. This preparation procedure was previously reported and it was found that under pyrolysis conditions, alginate is converted into a turbostratic graphitic carbon that upon exfoliation disperses into defective graphene with a residual oxygen

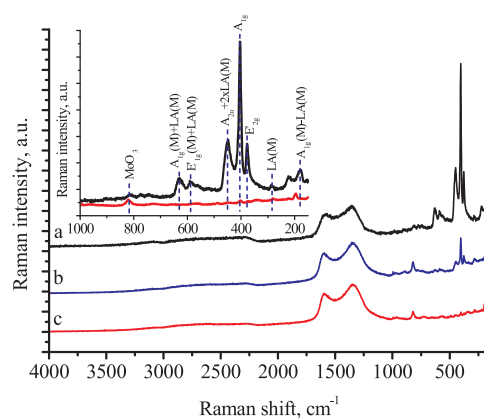


Fig. 6. Raman spectra of the fresh $\text{MoS}_2\text{-2/G}$ sample (a) and after being exposed to CO_2 at 500°C (b) or after its extensive use as CO_2 hydrogenation catalyst (c). Inset: $1000\text{--}200\text{ cm}^{-1}$ region for the fresh and spent sample.

content about 8% [35,36]. On the other hand, $(\text{NH}_4)_2\text{MoS}_4$ undergoes transformation into MoS_2 , occurring a spontaneous phase segregation under the conditions of the thermal treatment [29,30]. The strong grafting between the MoS_2 and the defective graphene phase is manifested by the 002 facet orientation and nanoplatelet morphology of the MoS_2 nanoparticles wetting the graphene sheets.

Three MoS_2/G samples containing different proportions of $(\text{NH}_4)_2\text{MoS}_4$ were prepared in order to determine the influence of MoS_2 content on the catalytic performance. Table 1 summarizes the MoS_2 content of the three MoS_2/G samples. It has been observed that MoS_2 loading determines the average size of MoS_2 nanoplatelets [30] and this parameter exerts generally a strong influence on the catalytic activity of

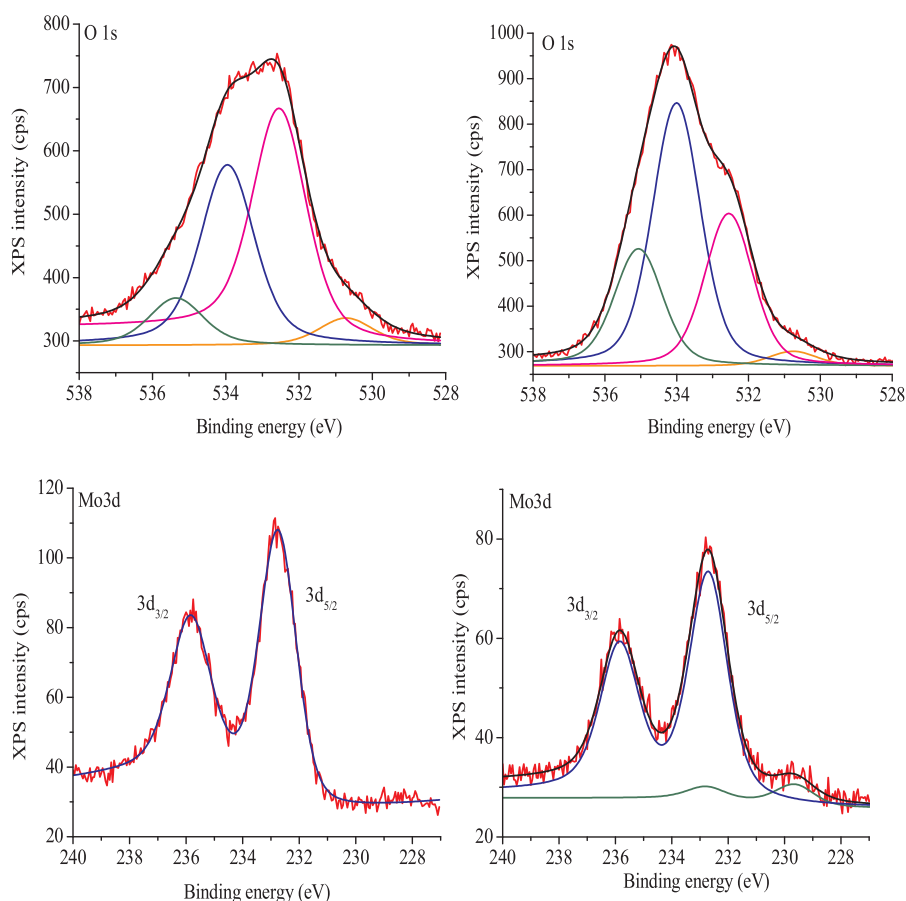


Fig. 5. XPS O 1s and Mo 3d peaks of the MoS_2/G catalyst fresh (left) and after being exhaustively used as CO_2 hydrogenation catalysts (right).

the materials.

Characterization data of MoS₂/G was in agreement with the literature. In particular, XRD patterns shown in Fig. S7 were in agreement with the formation of MoS₂ from (NH₄)₂MoS₄ during the pyrolysis, exhibiting a preferential orientation in the 002 facet, as reported [30]. This preferential orientation is reflected in the XRD pattern of the MoS₂/G by the presence of a strong peak corresponding to the diffraction in these 002 planes and the absence or negligible intensity of the diffraction in other crystallographic planes. In addition, Raman spectroscopy presents the three 2D, G and D peaks typical for defective G appearing at about 2750, 1590 and 1350 cm⁻¹, respectively. In addition, in the low frequency range, the E_g and A_{2g} vibrations due to the MoS₂ appearing about 410 and 380 cm⁻¹ were also recorded. Raman spectra will be further commented later when discussing MoS₂/G stability under reaction conditions.

SEM images of the MoS₂/G samples show that before exfoliation the material is constituted by an ensemble of thin platelets, while after sonication TEM images reveal the expected layered morphology for G of about 1–2 μm of lateral size with low contrast, on top of which the presence of smaller MoS₂ particles of lateral dimensions between 200–400 nm can be observed. Higher resolution of the MoS₂ particles shows the presence of few layers, in agreement with MoS₂ structure. Measurements of the interplanar distance in these nanoplatelets gives a value of 0.63 nm that is in agreement with the expected 002 interplanar distance of MoS₂ according to the data in the literature [37]. Fig. 1 presents a selection of SEM and TEM images to illustrate the morphology of the MoS₂/G catalyst.

The identity of the different particles, particularly the MoS₂ nanoplatelets, was firmly supported by EDX analysis that established the presence of Mo and S in these platelets with the expected 1.2 stoichiometry.

Preparation of the MoO₃/G samples is also illustrated in Scheme 1, while Table 1 contains relevant characterization data. In this case, the samples were obtained by adsorbing commercial MoO₃ nanoparticles on graphene previously obtained by pyrolysis of alginate and subsequent exfoliation by sonication [35]. Adsorption was carried out by suspending in water MoO₃ and graphene under continuous sonication, recovering the sample by filtration. Finally, MoO₃/G was exhaustively washed to remove weakly adsorbed nanoparticles. The maximum temperature at which MoO₃/G sample was submitted was 100 °C. Worth noting is that the particle size of MoO₃ is significantly smaller than that of MoS₂, what should favor the activity of MoO₃ over that of MoS₂. As in the previous case of MoS₂/G, three different samples containing increasing loadings of MoO₃ were prepared. The presence of MoO₃ on the graphene samples was assessed by XRD and by TEM images. Fig. 2 shows selected TEM images corresponding to the MoO₃/G sample at intermediate loading (6.2 wt%) where the presence of MoO₃ nanoparticles with average particle size about 22.8 nm was clearly observed on top of graphene sheet. It was noted that the average MoO₃ particle size increases with the MoO₃ content from about 15–40 nm, reflecting the occurrence of agglomeration of the primary nanoparticles as the percentage of MoO₃ increases. The MoO₃ loading was determined by ICP chemical analysis of the MoO₃ content, ranging from 0.5 to 11%.

3.2. Catalytic tests

As commented in the introduction, the purpose of the present study is to assess the catalytic activity of graphene supported Mo samples for CO₂ hydrogenation. A summary of the results for the set of samples at different reaction temperatures is presented in Table 1 and Fig. 3. As it can be seen there, in the range of temperatures under study from 250 to 500 °C, conversion of CO₂ increase with the reaction temperature, indicating that conversion at the experimental conditions is under kinetic control.

Blank controls in the absence of any catalyst shows that negligible CO₂ conversions occur in the absence of any catalyst in the range of

temperatures under study. The two products detected in all the experiments were methane and CO. When the reaction was carried out with graphene in the absence of Mo or with MoS₂ in the absence of graphene, CO was the major product, while for the MoS₂/G and MoO₃/G samples under study the major product was methane, frequently with selectivity above 95% and in some cases close to 100%. Thus, another control using as catalyst graphene, in the absence of any MoS₂ or MoO₃, also indicates a low conversion (about 6%) at the highest temperature under study, with a product distribution different to those when Mo compounds are present. It appears that graphene support exhibits some catalytic activity, in accordance with the known activity of graphene as metal-free hydrogenation catalyst of alkenes and nitro groups, among others [38–40]. It seems, however, that under the present conditions its contribution to CO₂ conversion is minor compared to that of Mo species that appear to be the active sites of CO₂ hydrogenation. The catalytic activity of bulk MoS₂ in the absence of graphene was also checked, observing a significant CO₂ conversion over 30% with almost complete selectivity towards CO. The results are compiled in Table S2 of the Supporting information. This selectivity towards CO sharply contrasts with that observed for the defective graphene supported Mo samples indicated in Table 1, for which CH₄ was the major product. This comparison between bulk MoS₂ and facet oriented MoS₂/G clearly reveals the role of strong support-MoS₂ interaction with defective graphene altering the reaction mechanism and determining a drastic change in product selectivity.

An influence of the Mo content on the catalytic activity was clearly observed. In the case of MoO₃/G, the catalytic activity increases along the Mo content, although not linearly. Thus, it was observed that the most active MoO₃/G sample was the one containing the highest MoO₃ content. However, the MoO₃/G sample with the MoO₃ loading as low as 0.5% was the one that exhibits the highest TOF values, indicating that the activity per Mo atom decreases upon loading increase. For these MoO₃ samples, CH₄ selectivity was above 99% except for reactions at 300 °C, for which CO was detected in somewhat higher selectivity, but always below 10%. Fig. S5 shows the variation of the Gibbs free energy with temperature for the hydrogenation of CO₂ for different H₂/CO₂ ratios. According to these variations a higher H₂/CO₂ ratio makes the reaction more favorable also favoring an increase in the selectivity to methane. The production of CO is favored at high temperatures. For the H₂/CO₂ ratio of 3 considered in our experiments the thermodynamic differences allows the production of both the CO and methane. Therefore, the difference in the selectivity is controlled by the catalyst and values measured for graphene, very different to those MoO₃/G samples, account for this.

In contrast to the case of MoO₃/G, the performance of MoS₂/G as a function of the MoS₂ content exhibits a volcano plot, there being an optimal amount of MoS₂ to achieve the highest CO₂ conversion between 25 and 33%, conversion decreasing as MoS₂ loading increases or decreases with respect to this range. This optimal loading is probably due to the compromise between two opposite factors influencing the catalytic performance. On one hand, the number of active sites due to MoS₂ should increase with loading, but, on the other hand, as previously discussed, particle size also increases with loading. For this reason a balance between small particle size and number of sites is reached at intermediate MoS₂ loading. With regard to selectivity to methane, it was observed that methane selectivity for MoS₂/G was significantly lower than the values for MoO₃/G, and particularly at low temperatures and low CO₂ conversions, CO selectivities over 10% were measured. This is again the effect of a kinetic controlled effect.

The deposition of MoS₂ and MoO₃ onto graphene changed the previously reported order of the activity [19], MoS₂ being more active. However, the methanation was almost complete on MoO₃/G compared to MoS₂/G on which part of the CO₂ was reduced only to CO.

Table 2 compiles values of the Weisz-Prater criterion for differential reaction conditions (CO₂ conversion < 5%, P = 10 bar, CO₂:H₂ (vol) = 1:3). The values of Table 2 show a very good agreement

between Chapman-Enskog (C-E) and Wilke-Lee (W-L) approaches and experimental results. Thus, for $D_{\text{CO}_2\text{-H}_2}$ C-E: 0.531, W-L: 0.505, and exp.: $0.55 \text{ cm}^2/\text{s}$, and for $D_{\text{CO}_2\text{-CH}_4}$ C-E: 0.141, W-L: 0.150, and exp.: $0.153 \text{ cm}^2/\text{s}$. The values of the diffusion coefficients for the reactants in the gas reaction mixture ($D_{\text{CO}_2,\text{m}}$ and $D_{\text{H}_2,\text{m}}$) calculated using Blanc's law are presented in the same Table 2.

The reaction rate was calculated for differential reaction conditions (CO_2 conversion < 5%) where, for low X_i values, the formula (6) of the conversion rate in a packed-bed plug flow reactor (PFR) [41] becomes approximately equal to (7) that describes the mass balance of a continuous tank stirred reactor (CSTR), allowing thus a simple calculation of CO_2 consumption rates ($-r_i$) listed in Table 2. The high selectivity values in CH_4 indicate that the prevalent occurring reaction is $\text{CO}_2 + 4\text{H}_2 = \text{CH}_4 + 2\text{H}_2\text{O}$ and, thus, the consumption rate of H_2 has been approximated as four times the consumption rate of CO_2 .

$$\frac{m_L}{(F_0)_i} = \int_0^{X_A} \frac{dX_i}{-r_i} \quad (6)$$

$$\frac{m_L}{(F_0)_i} = \frac{X_i}{-r_i} \quad (7)$$

where:

m_L = mass of catalyst, g
 F_0 = molar flow rate, mol/s
 X_i = fractional conversion of reactant i
 r_i = molar rate of reactant i consumption, per unit mass of catalyst, mol/(s·g)
 $-r_i$ = average specific rate of reactant i consumption in the conversion range $[0, X_i]$ Particle radii and bulk catalyst densities are: $\text{MoS}_2\text{-1/G}$ - $1.375 \cdot 10^{-5} \text{ cm}$; 0.289 g cm^{-3} , $\text{MoS}_2\text{-2/G}$ - $1.5 \cdot 10^{-5}$; 0.247 , $\text{MoS}_2\text{-3/G}$ - $1.5 \cdot 10^{-5}$; 0.276 , $\text{MoS}_2\text{-4/G}$ - $1.75 \cdot 10^{-5}$; 0.337 , $\text{MoO}_3\text{-1/G}$ - $0.75 \cdot 10^{-6}$; 0.233 , $\text{MoO}_3\text{-2/G}$ - $1.15 \cdot 10^{-6}$; 0.256 , $\text{MoO}_3\text{-3/G}$ - $2.05 \cdot 10^{-6}$; 0.310 .

The concentration of the reactants at the surface of the catalyst has been considered the same as in the gas mixture due to the low values of the space velocities and pressure/temperature values used during the experiments. Critical parameters were used to determine the a and b Van der Waals constants of pure gases that were summed according to the mixing rules described by Hirschfelder et al. [31] to obtain the a and b constants of the pentacomponent gas reaction mixtures. The molar volume was further calculated from the Van der Waals equation of state. Slightly larger values compared to the application of the ideal gas equation of state were determined indicating thus a very small prevalence of the repulsive inter-molecular forces. The ratio between the mole fraction of the reactant and the molar volume allows to the reactant concentrations listed in Table 2.

Very important to notice, all values of the Weisz-Prater criterion calculated for the experiments occurring in differential reactions conditions (Table 2) are by far smaller than 0.3 indicating that no mass transfer limitations affect the ongoing catalytic reactions.

From the influence of the temperature on CO_2 conversion, apparent activation energies (E_a) were calculated (Fig. 4). The results show a variation of E_a values from 115 ± 15 to $79 \pm 12 \text{ kJ} \times \text{mol}^{-1}$ depending on the nature of the Mo catalyst and its loading. These E_a values are in the range reported for other catalysts [42,43].

Catalyst stability was studied by carrying out a series of experiments in where under the same space velocity, the temperature of the reaction was increased from 300 to 500 °C and then, decreased again, observing in the case of MoO_3/G constantly reproducible catalytic data, while in the case of MoS_2/G some minor decay in activity upon time of stream was observed (Fig. S6). XPS characterization of the samples before and after using the materials as catalysts for CO_2 hydrogenation showed no difference in the case of MoO_3/G , in agreement with the notable stability of these samples. In the case of MoS_2/G , some changes in the Mo 3d peak were observed in the MoS_2/G sample submitted to exhaustive

use as catalyst in the CO_2 hydrogenation that are compatible with the formation of some Mo(VI) component in about 20%. Fig. 5 presents the XPS Mo 3d and O 1s peaks of the MoS_2/G sample fresh and after its use as CO_2 hydrogenation catalyst, where the remarkable changes in the shape and distribution of the O 1s peak can be seen, as well as the appearance in Mo 3d of a component attributable to oxidized Mo^{VI} [44–47]. It should be commented at this point that also bulk MoS_2 is not completely stable under the reaction conditions according to XRD, where the presence of some additional diffraction peaks after the use of the material as hydrogenation catalyst can be observed (see Fig. S9 in the Supporting information).

Raman spectroscopy indicates that the changes in MoS_2 are most likely associated to the conversion of some MoS_2 in the corresponding MoO_x oxide, based on the appearance of a new vibration band at 810 cm^{-1} [48]. Fig. 6 illustrates these changes in the spent MoS_2/G respect to the fresh sample or even to the MoS_2/G exposed to CO_2 that should be responsible for oxidation of MoS_2 , whereby the decrease or disappearance of the peaks associated to MoS_2 at 380, 407, 450, 590 and 630 cm^{-1} [49] are accompanied with the appearance of the characteristic MoO_x band. Thus, it seems that the most likely cause of MoS_2/G instability is the partial reaction of MoS_2 with CO_2 causing some oxidation from Mo(IV) of MoS_2 to Mo(VI) and transformation to the oxide.

4. Conclusions

The present study has shown that MoS_2 supported on defective graphene derived from biomass is a selective catalysts for CO_2 methanation, increasing the catalytic activity with the temperature in the range from 300 to 600 °C. This catalytic activity sharply contrasts with that of bulk MoS_2 for which CO is the major product and reflects the important role of graphene on the activity of supported Mo species. There is an influence of the MoS_2 loading on graphene on the performance of the catalyst, there being an optimal MoO_3 exhibits a remarkable activity and stability, while MoS_2 undergoes some desulfuration under the reaction conditions and partial oxidation. It appears that the particle size is a critical parameter controlling the catalytic activity in the case of MoS_2/G prepared in a single pyrolysis step and that this limits the maximum loading of MoS_2 that can be deposited on the graphene. In the case of MoO_3 nanoparticles, their average particle size is not altered in the adsorption process and, consequently, higher loadings of 10 nm particles can be achieved, this resulting in an increasing catalytic activity as the loading increases in the range of 11 wt.%. The deposition of MoS_2 or MoO_3 onto graphene led to a different catalytic behavior compared to previously reported bulk catalysts, MoS_2 being more active than MoO_3 . However, the methanation was almost complete on MoO_3/G compared to MoS_2/G on which part of the CO_2 was reduced only to CO. These results illustrate the potential of graphene as support of active molybdenum species in gas-phase hydrogenations.

Acknowledgements

Vasile I. Parvulescu kindly acknowledges UEFISCDI for financial support (project PN-III-P4-ID-PCE-2016-0146, Nr. 121/2017 and project PN-III-P1-1.2-PCCDI-2017-0541). Financial support by the Spanish Ministry of Economy and Competitiveness (Severo Ochoa and CTQ2015-69653-CO2-R1) and Generalitat Valencia (Prometeo 2017-083) is gratefully acknowledged. A.P. also thanks the Spanish Ministry for a Ramon y Cajal research associate contract.

Appendix A. Supplementary data

Supplementary material related to this article can be found, in the online version, at doi:<https://doi.org/10.1016/j.apcatb.2018.12.034>.

References

- [1] M. Aresta, Carbon Dioxide as Chemical Feedstock, John Wiley & Sons, 2010.
- [2] A. Corma, H. García, Photocatalytic reduction of CO₂ for fuel production: possibilities and challenges, *J. Catal.* 308 (2013) 168.
- [3] C.-H. Huang, C.-S. Tan, A review: CO₂ utilization, *Aerosol Air Qual. Res.* 14 (2) (2014) 480.
- [4] M. Aresta, A. Dibenedetto, A. Angelini, The changing paradigm in CO₂ utilization, *J. Co₂ Util.* 3 (2013) 65.
- [5] S. Saeidi, N.A.S. Amin, M.R. Rahimpour, Hydrogenation of CO₂ to value-added products—a review and potential future developments, *J. Co₂ Util.* 5 (2014) 66.
- [6] H. Arakawa, Studies in Surface Science and Catalysis vol. 114, Elsevier, 1998.
- [7] J.I. Levene, M.K. Mann, R.M. Margolis, A. Milbrandt, An analysis of hydrogen production from renewable electricity sources, *Solar Energy* 81 (6) (2007) 773.
- [8] K.-A. Adamson, Hydrogen from renewable resources—the hundred year commitment, *Energy Policy* 32 (10) (2004) 1231.
- [9] M. Beaudin, H. Zareipour, A. Schellenberg, W. Rosehart, Energy storage for mitigating the variability of renewable electricity sources: an updated review, *Energy Sustain. Dev.* 14 (4) (2010) 302.
- [10] W. Wang, S. Wang, X. Ma, J. Gong, Recent advances in catalytic hydrogenation of carbon dioxide, *Chem. Soc. Rev.* 40 (7) (2011) 3703.
- [11] C. Federsel, R. Jackstell, M. Beller, State-of-the-art catalysts for hydrogenation of carbon dioxide, *Angew. Chem. Int. Ed.* 49 (36) (2010) 6254.
- [12] M.A. Banares, Supported metal oxide and other catalysts for ethane conversion: a review, *Catal. Today* 51 (2) (1999) 319.
- [13] G.M. Dhar, B. Srinivas, M. Rana, M. Kumar, S. Maity, Mixed oxide supported hydrodesulfurization catalysts—a review, *Catal. Today* 86 (1–4) (2003) 45.
- [14] J. Volta, J. Portefaix, Structure sensitivity of mild oxidation reactions on oxide catalysts—a review, *Appl. Catal.* 18 (1) (1985) 1.
- [15] P. Grange, B. Delmon, The role of cobalt and molybdenum sulphides in hydrodesulphurisation catalysts: a review, *J. Less Common Met.* 36 (1–2) (1974) 353.
- [16] S. Zaman, K.J. Smith, A review of molybdenum catalysts for synthesis gas conversion to alcohols: catalysts, mechanisms and kinetics, *Catal. Rev.* 54 (1) (2012) 41.
- [17] F. Meng, J. Li, S.K. Cushing, M. Zhi, N. Wu, Solar hydrogen generation by nanoscale p–n junction of p-type molybdenum disulfide/n-type nitrogen-doped reduced graphene oxide, *J. Am. Chem. Soc.* 135 (28) (2013) 10286.
- [18] Y. Liu, H. Wu, H.-C. Cheng, S. Yang, E. Zhu, Q. He, M. Ding, D. Li, J. Guo, N.O. Weiss, Toward barrier free contact to molybdenum disulfide using graphene electrodes, *Nano Lett.* 15 (5) (2015) 3030.
- [19] M. Saito, R.B. Anderson, The activity of several molybdenum compounds for the methanation of CO₂, *J. Catal.* 67 (2) (1981) 296.
- [20] S. Yao, L. Gu, C. Sun, J. Li, W. Shen, Combined methane CO₂ reforming and dehydroaromatization for enhancing the catalyst stability, *Ind. Eng. Chem. Res.* 48 (2) (2008) 713.
- [21] H. Li, L. Wang, Y. Dai, Z. Pu, Z. Lao, Y. Chen, M. Wang, X. Zheng, J. Zhu, W. Zhang, et al., Synergetic interaction between neighbouring platinum monomers in CO₂ hydrogenation, *Nat. Nanotechnol.* 13 (5) (2018) 411.
- [22] P. Liu, Y. Choi, Y. Yang, M.G. White, Methanol synthesis from H₂ and CO₂ on a Mo₆S₈ cluster: a density functional study, *J. Phys. Chem. A* 114 (11) (2009) 3888.
- [23] M. Huang, K. Cho, Density functional theory study of CO hydrogenation on a MoS₂ surface, *J. Phys. Chem. C* 113 (13) (2009) 5238.
- [24] X. Liu, Y. Song, W. Geng, H. Li, L. Xiao, W. Wu, Cu-Mo₂C/MCM-41: an efficient catalyst for the selective synthesis of methanol from CO₂, *Catalysts* 6 (5) (2016) 75.
- [25] S. Posada-Pérez, P.J. Ramírez, J. Evans, F. Viñes, P. Liu, F. Illas, J.A. Rodríguez, Highly active Au/δ-MoC and Cu/δ-MoC catalysts for the conversion of CO₂: the metal/C ratio as a key factor defining activity, selectivity, and stability, *J. Am. Chem. Soc.* 138 (26) (2016) 8269.
- [26] Y. Shi, Y. Yang, Y.-W. Li, H. Jiao, Activation mechanisms of H₂, O₂, H₂O, CO₂, CO, CH₄ and C₂H₄ on metallic Mo₂C (001) as well as Mo/C terminated Mo₂C (101) from density functional theory computations, *Appl. Catal. A: Gen.* 524 (2016) 223.
- [27] M.D. Porosoff, J.W. Baldwin, X. Peng, G. Mpourmpakis, H.D. Willauer, Potassium-promoted molybdenum carbide as a highly active and selective catalyst for CO₂ conversion to CO, *ChemSusChem* 10 (11) (2017) 2408.
- [28] N. Li, X. Chen, W.-J. Ong, D.R. MacFarlane, X. Zhao, A.K. Cheetham, C. Sun, Understanding of electrochemical mechanisms for CO₂ capture and conversion into hydrocarbon fuels in transition-metal carbides (MXenes), *ACS Nano* 11 (11) (2017) 10825.
- [29] M. Latorre-Sánchez, I. Esteve-Adell, A. Primo, H. García, Innovative preparation of MoS₂–graphene heterostructures based on alginate containing (NH₄)₂MoS₄ and their photocatalytic activity for H₂ generation, *Carbon* 81 (2015) 587.
- [30] J. He, C. Fernández, A. Primo, H. García, One-step preparation of large area films of oriented MoS₂ nanoparticles on multilayer graphene and its electrocatalytic activity for hydrogen evolution, *Materials* 11 (1) (2018) 168.
- [31] B.E. Poling, J.M. Prausnitz, J.P. O'connell, The Properties of Gases and Liquids, McGraw-Hill, New York, 2001.
- [32] D.W. Green, Perry's Chemical Engineers, McGraw Hill, 2008.
- [33] M.A. Vannice, W.H. Joyce, Kinetics of Catalytic Reactions, Springer, 2005.
- [34] H.S. Fogler, Elements of Chemical Reaction Engineering, (1999).
- [35] A. Dhakshinamoorthy, A. Primo, P. Concepcion, M. Alvaro, H. García, Doped graphene as a metal-free carbocatalyst for the selective aerobic oxidation of benzylic hydrocarbons, cyclooctane and styrene, *Chem. Eur. J.* 19 (23) (2013) 7547.
- [36] M.M. Trandafir, M. Florea, F. Neațu, A. Primo, V.I. Parvulescu, H. García, Graphene from alginate pyrolysis as a metal-free catalyst for hydrogenation of nitro compounds, *ChemSusChem* 9 (13) (2016) 1565.
- [37] J. Xie, H. Zhang, S. Li, R. Wang, X. Sun, M. Zhou, J. Zhou, X.W.D. Lou, Y. Xie, Defect-rich MoS₂ ultrathin nanosheets with additional active edge sites for enhanced electrocatalytic hydrogen evolution, *Adv. Mater.* 25 (40) (2013) 5807.
- [38] Y. Gao, D. Ma, C. Wang, J. Guan, X. Bao, Reduced graphene oxide as a catalyst for hydrogenation of nitrobenzene at room temperature, *Chem. Commun.* 47 (8) (2011) 2432.
- [39] H. Hu, J.H. Xin, H. Hu, X. Wang, Y. Kong, Metal-free graphene-based catalyst-insight into the catalytic activity: a short review, *Appl. Catal. A: Gen.* 492 (2015) 1.
- [40] A. Primo, F. Neațu, M. Florea, V. Parvulescu, H. García, Graphenes in the absence of metals as carbocatalysts for selective acetylene hydrogenation and alkene hydrogenation, *Nat. Commun.* 5 (2014) 5291.
- [41] R.W. Missen, C.A. Mims, B.A. Saville, Introduction to Chemical Reaction Engineering and Kinetics, Wiley, New York, 1999.
- [42] G.D. Weatherbee, C.H. Bartholomew, Hydrogenation of CO₂ on group VIII metals: II. Kinetics and mechanism of CO₂ hydrogenation on nickel, *J. Catal.* 77 (2) (1982) 460.
- [43] G.D. Weatherbee, C.H. Bartholomew, Hydrogenation of CO₂ on group VIII metals: I. Specific activity of NiSiO₂, *J. Catal.* 68 (1) (1981) 67.
- [44] J. Haber, T. Machej, L. Ungier, J. Ziolkowski, ESCA studies of copper oxides and copper molybdates, *J. Solid State Chem.* 25 (3) (1978) 207.
- [45] M. Smith, U. Ozkan, The partial oxidation of methane to formaldehyde: role of different crystal planes of MoO₃, *J. Catal.* 141 (1) (1993) 124.
- [46] J. Wei, Z. Yin, S.-C. Chen, D. Cai, Q. Zheng, Solution-processed MoS_x thin-films as hole-transport layers for efficient polymer solar cells, *RSC Adv.* 6 (45) (2016) 39137.
- [47] B. Brox, I. Olefjord, ESCA studies of MoO₂ and MoO₃, *Surf. Interface Anal.* 13 (1) (1988) 3.
- [48] M. Dieterle, G. Mestl, Raman spectroscopy of molybdenum oxides part II. Resonance Raman spectroscopic characterization of the molybdenum oxides Mo₄O₁₁ and MoO₂, *J. Chem. Soc. Faraday Trans.* 4 (5) (2002) 822.
- [49] K. Gołasa, M. Grzeszczyk, K. Korona, R. Bożek, J. Binder, J. Szczytko, A. Wysmołek, A. Babiński, Optical properties of molybdenum disulfide (MoS₂), *Acta Phys. Pol. A* 124 (5) (2013).